WACMOS-ET – LST Product

Algorithm Theoretical Basis Document

João Paulo Martins

Isabel Franco Trigo

Ana Cordeiro Pires

Instituto Português do Mar e da Atmosfera

2014

Contents

1 Summary

This document describes the production of the Land Surface Temperature (LST) datasets, which are the main deliverables of the WP2110 part of the WACMOS-ET project. LST is calculated from L1 radiances from AATSR, onboard ESA's EnviSAT polar-orbiting satellite, from MTSAT-2 (over Australia), MSG-2 and GOES-12 (full disks). The datasets are reported over a sinusoidal grid with 1km resolution for AATSR and 5km for the remaining sensors. The algorithm that was chosen for AATSR, MTSAT and MSG is a generalized split-windows model, which requires radiances from the 10.8 µm and 12 µm channels and uses time-varying spectral emissivities and total column water vapor (TCWV) from ECMWF fields. The choice of the algorithm is discussed, based on an intercomparison of models documented in the literature. The models were calibrated and validated using a database of clear-sky profiles of temperature and humidity and respective surface conditions and a radiative transfer model to simulate TOA brightness temperatures. The choice of algorithm was also based on the way input errors propagate on each model: sensitivities to sensor noise, emissivity and TCWV were evaluated and the final error is reported as a function of the TCWV and emissivity. For GOES, a new mono-channel algorithm with dynamic emissivity was developed and evaluated, since no 12 µm radiances are available on that sensor.

2 Introduction

Land Surface Temperature (LST) is a key parameter of the surface radiative budget, as it measures the available energy at the surface-atmosphere interface. LST is a useful quantity for the scientific community, namely for those dealing with weather and climate numerical models. Accurate values of LST are also of special interest in a wide range of areas related to land surface processes, including meteorology, hydrology, agrometeorology, climatology and environmental studies. LST is very difficult to quantify, even with in situ measurements, due to its high temporal and spatial variability as well as to strong directional effects. Radiometers are often used over controlled sites with well-known surface properties and these measurements closely match those obtained by remote sensing techniques (Trigo, et al. 2008b).

The Satellite Application Facility on Land Surface Analysis (Land-SAF), as part of the ground segment of the European Organization for the Exploitation of Meteorological Satellites (EUMETSAT), generates LST from the Spinning Enhanced Visible and Infrared Imager (SEVIRI) onboard Meteosat Second Generation (MSG) satellites, on an operational basis since March 2005 (Trigo et al. 2011, Schmetz et al. 2002). The Land-SAF operational LST retrieval algorithm uses a generalized split-window technique (GSW), which performs corrections for atmospheric effects based on the differential absorption in adjacent IR bands on cloud-free pixels. There are a number of available GSW formulations (see section 3); Land-SAF adopted the one originally developed by Wan and Dozier (1996) for Moderate Resolution Imaging Spectroradiometer (MODIS), and later adapted to the Spinning Enhanced Visible and Infrared Imager (SEVIRI) by Trigo et al. (2008b) and Freitas et al. (2010). Surface temperature is estimated as a linear function of clear-sky TOA brightness temperatures for the split-window channels 10.8 μm and 12.0 μm, where regression coefficients depend explicitly on land surface emissivity for each channel, and implicitly on atmospheric total column water vapor (TCWV) and zenith viewing angle (ZVA).

Within the WACMOS-ET framework, based on the Land-SAF formulation and besides the LST product from SEVIRI/MSG, operationally provided by the Land-SAF since 2005

(Trigo et al. 2011), similar methodologies are evaluated in order to produce LST for three other sensors: polar-orbiter Advanced Along-Track Scanning Radiometer (AATSR), and geostationary Multi-function Transport Satellite (MTSAT) and Geostationary Operational Environmental Satellite (GOES). Geostationary satellites provide a better sampling of diurnal cycle surface temperature under clear sky conditions, despite the limited area coverage and coarser spatial resolution when compared to products derived from polar-orbiters. LST products from these platforms are being provided in near real time since 2010 (Lacaze et al. 2010), being part of the current Copernicus Global Land Service (http://copernicus.eu/pages-principales/services/land-monitoring/).

Furthermore, a new method is evaluated, that includes an explicit dependence on the ZVA, through the introduction of a new term in the regression. This term has been shown to accurately take the ZVA variability into account on the LST calculation (Yu et al. 2008). In this document, several GSW formulations are compared in terms of algorithm accuracy and sensitivity to input errors. A similar model intercomparison was done by Yu et al. (2008), and the same GSW formulations used therein are used here.

The LST error is quantified as a sum of the contributions of the sensor noise, uncertainties in the surface emissivity and in the TCWV forecasts (see section 3.3). A framework similar to the one used by Freitas et al. (2010) is used to characterize the error of each of the individual inputs on the different GSWs. The LST error is computed for all sensors except SEVIRI/MSG, since the data used is that provided by the Land-SAF operational chain and the error computation is only available from July 2008 onwards, which is mostly out of the WACMOS-ET study period as detailed below.

3 Sensor characteristics and currently used products

3.1 AATSR

One of WACMOS-ET main goals is to demonstrate the use AATSR-derived LST fields for the estimation and/or as complementary information of evapotranspiration. AATSR was one of the 10 Earth-observing instruments on-board ESA's polar orbiter EnviSAT (ENVIronment SATellite), launched on March 2002. Its mission ended in 2012. Like its predecessors from the ATSR series, it includes dual-view scanner: it swaths a given scene in the forward view (ZVA ranging from 52.4º to 55º) and 150 s later, or when the satellite has moved approximately 1000 km forward along the ground track, it observes the same in the nadir view (with ZVA ranging from 0º to 21.6º) (Soria and Sobrino 2007). Pixel size in the nadir view is 1 km by 1 km, but 1.5 km by 2 km in the forward view. The sensor has 7 bands in the visible, near and thermal infrared, with central wavelengths at 0.56, 0.66, 0.86, 1.6, 3.7, 10.9 and 12.1 μm. The response function of the split-window channels is shown on Figure 1 (as well as the ones from the remaining instruments used in this project).

The AATSR was initially designed to provide sea surface temperature (SST) maps, ensuring the production of a unique 10 year near-continuous data set at the levels of accuracy required (0.3 K or better). However, nowadays AATSR data is being used more and more to obtain LST on a global scale. A Level 2 LST product is currently provided by ESA according to the AATSR Algorithm Theoretical Basis Document (Prata 2002). The algorithms proposed to produce the Level 2 LST images of the AATSR sensor use pixel-by-pixel top-of-the-atmosphere cloud-free, calibrated and navigated day and night brightness temperatures from the 11 and 12 μm AATSR channels. This algorithm also requires as inputs the following parameters: seasonally-dependent land cover classification, fractional vegetation and precipitable water. The first two were determined using the biomes provided by Dorman and Sellers (1989) from a grid of 1°×1° resolution. The precipitable water data was based on the NVAP climatology at 2.5°×2.5° resolution and monthly intervals. This spatial resolution for both fractional cover and precipitable water is currently one of the main problems in the retrieval of the LST.

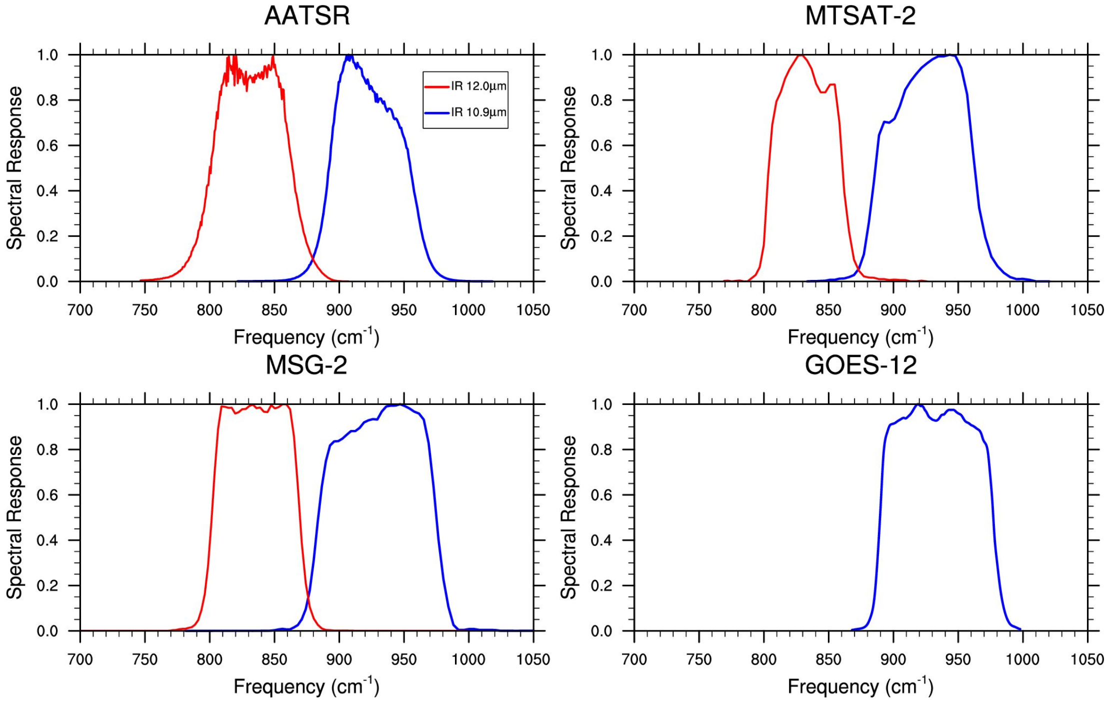

Figure 1 - Spectral response functions for the split-window channels 10.9 µm and 12.0µm for AATSR, MTSAT, MSG and GOES. For the latter, no 12 µm channel is available.

The WACMOS-ET project plans to tackle some of these issues by using a new approach, similar to the one used to produce the Land-SAF operational LST product: precipitable water will be taken from the ERA-Interim reanalysis (Dee et al. 2011), and surface emissivity was taken from the Global Infrared Land Surface Emissivity UW-Madison Baseline Fit Emissivity Database developed by Seeman et al. (2008), which provides global spectral emissivities for each month with 0.05º spatial resolution.

3.2 SEVIRI/MSG

Meteosat Second Generation (MSG) is a joint project between ESA and the European Organisation for the Exploitation of Meteorological Satellites (Eumetsat) and follows up the success of the first generation Meteosat weather satellite series (MFG). The first MSG satellite was launched in August 2002, entering into service with Eumetsat in early 2004 and now renamed Meteosat-8. The second MSG, Meteosat-9, was launched on 21 December 2005 and MSG-3 (Meteosat-10) was launched on 5 July 2012. Their location is 3.5ºE, 9.5ºE, and 0ºE, respectively. MSG-3 is currently the prime operational geostationary satellite.

The operational Land-SAF LST is available with a 15 minute temporal frequency and at the original satellite spatial resolution (3 km sampling distance at the sub-satellite point) and geostationary projection. The data are available in near real time and off-line since January 2005 for Europe and for the whole SEVIRI disk from July 2005. The SEVIRI sensor encompasses 12 channels covering the visible to the infrared (Schmetz et al., 2002a). For further information please refer to Freitas et al. (2010) and the documentation on the Land-SAF website (http://landsaf.ipma.pt/algorithms.jsp).

3.3 MTSAT

MTSAT-2 is the Japanese Meteorological Association (JMA) Multifunction Transport SATellite launched in February 2006, following the MTSAT-1R launched one year prior. Both MTSATs are geostationary satellites centered at 140ºE and 145ºE, respectively. The Japanese Advanced Meteorological Imager (JAMI) onboard MTSAT-2 (the mission currently in place) has the following channels: near-visible IR at 0.55 µm to 0.90 µm; medium IR1 at 3.5 µm to 4.0 µm; medium IR2 at 6.5 µm to 7.0 µm; thermal IR1 at 10.3 µm to 11.3 µm; and thermal IR2 at 11.5 µm to 12.5 µm. LST is computed based on the information provided by the two thermal IR channels, which have a spatial resolution of 4 x 4 km and a temporal resolution of 3 hours.

The MTSAT sensor data disseminated via EUMETCast does not include brightness temperatures for the TIR2 channel, and so the LST product that is being generated operationally by the Copernicus Global Land Service follows a methodology tailored to the MTSAT response functions of MIR and TIR1 channels (Freitas et al., 2013). Within the framework of WACMOS-ET, we are processing MTSAT data for an area covering Australia and for period June 2006-December 2007, where both TIR channels are available. In this way, we are able to apply a generalized split-window formulation similar to that derived for AATSR and SEVIRI.

3.4 GOES

GOES-12 was launched in July 2001. In April 2003, GOES-12 became GOES-East at 75ºW, and was decommissioned in April 2010. Its mission ended August 2013. GOES-12 was the last of the third generation GOES satellites. In contrast to SEVIRI, AATSR and

MTSAT, the imager onboard GOES satellites (from GOES-12 onwards, http://www.oso.noaa.gov/goes/goes-calibration/change-channels.htm) does not include two channels in the thermal atmospheric window of the spectrum (Table 1). Alternative methodologies to the split-window algorithms must then be applied in order to obtain LST, as detailed in section 3.2.

Table 1 – Window channels in the infrared domain, available on geostationary platforms.

	SEVIRI	GOES	MTSAT
MIR	3.5 – 4.4 µm	3.8 – 4.0 µm	3.5 – 4.0 µm
TIR1	10.0 – 11.5 µm	10.2 – 11.2 µm	10.3 – 11.3 µm
TIR2	11.2 – 12.8 µm	-	11.5 - 12.5 µm(*)

(*) Not disseminated via EUMETCast.

4 Algorithms

4.1 Calibration and Verification Database

LST is to be estimated using a split-windows formulation with surface emissivity as an explicit input. The split-window coefficients are trained and verified for a wide range of atmospheric and surface conditions and viewing geometries, using the MODerate spectral resolution atmospheric TRANSmittance model (MODTRAN; Berk et al. 2000) simulations for the more than 15700 clear sky profiles available in the database prepared by Borbas et al. (2005), referred to as SeeBor.

The algorithm (MODTRAN4) provides a useful tool to quantify the radiation emitted by the surface within known atmospheric conditions that reaches a sensor operating in a specific spectral band. The radiance, L_v, is estimated using MODTRAN4, for the bands corresponding to IR 108 and IR 120 channels, with a spectral resolution of 1 cm^{-1}. The integration of L_v weighted by the ith channel response function $\phi_{i,v}$ provides its effective radiance:

$$L_i = \frac{\int_{\nu_{i,1}}^{\nu_{i,2}} \phi_{i,\nu} L_\nu d\nu}{\int_{\nu_{i,1}}^{\nu_{i,2}} \phi_{i,\nu} d\nu} \quad (1)$$

where $\nu_{i,1}$ and $\nu_{i,2}$ are the lower and upper wavenumber boundaries of the channel, respectively; the integrals in (1) are estimated by taking into account the full tabulated values of the response function $\phi_{i,\nu}$. Table 2 shows these wavenumbers for all sensors, for both IR channels.

Table 2 – Wavenumber boundaries of both IR channels of AATSR and MTSAT.

	ν_1 (cm^{-1})		ν_2 (cm^{-1})	
IR channel	**IR 108**	**IR 120**	**IR 108**	**IR 120**
AATSR	821.60	746.66	1018.32	907.12
SEVIRI	783.70	716.33	1131.22	996.02
MTSAT	833.33	769.23	1020.40	925.90
GOES	862.80	--	1000.50	--

The simulated radiances for channel i, i.e. L_i's, are then converted to equivalent black-body brightness temperatures ($Tb_{,i}$) following the analytic formulation based on the Planck function:

$$Tb_i = \frac{C_2 \nu_{i,c}}{\log\left(\frac{C_1 \nu_{i,c}^3}{L_i} + 1\right)} \quad (2)$$

where $\nu_{i,c}$ is channel i central wavenumber, $C_1=2hc^2$, and $C_2=hc/k$ (with h being the Planck's constant, c being the speed of light, and k being the Boltzmann constant).

The SeeBor database includes the necessary information about atmospheric temperature and humidity, surface emissivity, skin temperature, pressure, total column water vapor and land cover and height. The simulations took into account the respective channel response function (Figure 1). For each profile, a random ZVA is assumed; for AATSR the angle interval is within the range of the nadir FOV (0º - 21.6º), while for the geostationary satellites the interval includes angles up to 75º for MTSAT and 60º for GOES, comprising most of the disk. A subset of this dataset was used to produce a calibration database, with 80 profiles that were geographically well distributed and with a uniform TCWV distribution in order to cover a wide range of atmospheric conditions (Figure 2). For each of these profiles, the skin temperature was perturbed by taking the 10 m temperature and adding perturbations in the range [-15 15] in 5 K intervals. Each of these cases was modelled using the following ZVA intervals: in the range 0-22º in 1º intervals for AATSR; in the range 0-75º in 5º intervals for MTSAT and 0-60º in 5º intervals for GOES. For computational reasons, each case was initially run with a constant emissivity of 0.5, which is later corrected for each channel as follows: the emissivity of the IR 12.0 channel is set to vary between 0.95 and 0.995 in 0.015 intervals. For each of these values, the IR 10.8 emissivity is calculated by adding perturbations in the range [-0.24 0.24] in 0.006 intervals (excluding cases where it exceeds 1). This is valid for all sensors except SEVIRI, because it was already calibrated and validated before the project started. The following range of variability was used for SEVIRI: channel emissivities of TIR1 and TIR2 (ε_{TIR1} and ε_{TIR2}, respectively) cover the range $0.96<\varepsilon_{TIR2}<0.995$ in steps of 0.0175 and $\varepsilon_{TIR2}-0.030 < \varepsilon_{TIR1} <\varepsilon_{TIR2}+0.018$ in steps of 0.006 (excluding cases with the average of ε_{TIR1} and ε_{TIR2} below 0.94). In this way, one can be sure the database is robust in respect to atmospheric conditions, differences between skin and 10 m temperature, ZVA and also to the average and difference between the emissivities of the split-window channels. The remaining profiles in the database were used for validation of the calibrated coefficients, using random ZVAs, as described above.

4.2 Description of the LST algorithms

A set of GSW formulations was intercompared by Yu et al. (2008). In general, these equations reflect that LST is a function of the top-of-atmosphere (TOA) brightness temperatures and surface emissivities, in the split window channels (Table 3). They were typically developed with different assumptions and approximations and tested under different environmental conditions. As the theoretical underpinnings are not germane to this study, the readers are referred to the original publications for their development details.

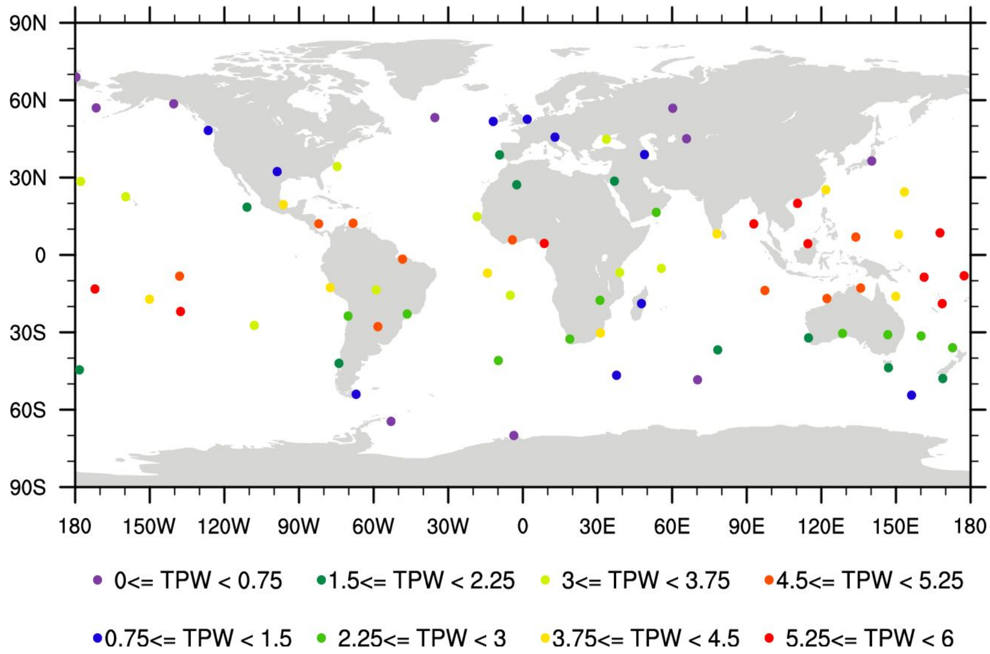

Figure 2 - Location of the calibration profiles, colored by TCWV (cm).

There are several approaches to introduce a degree of dependence of the atmospheric correction due to increasing optical path with viewing angle and total column water vapor. Some operational algorithms use coefficients that are regressed over TCWV and ZVA classes (e.g. Freitas et al. 2010). This method has some disadvantages in terms of the resulting LST fields, as spatial discontinuities are often produced when neighboring coefficients are used in adjacent regions. As proposed and tested by Yu et al. (2008), a correction term proportional to the temperature difference between the SW channels – which accounts for the increasing optical path with water vapor – and to (*sec* θ – 1) – *θ* being the ZVA – which represents the path difference from the nadir, i.e. a term with a form

$$B(T_{11}-T_{12})(\sec\theta-1), \qquad (3)$$

where *B* is a new regression coefficient that may be added to each of the SW formulations on Table 3. Here, both approaches were compared for AATSR: in the approach (a), coefficients were derived for TCWV classes from 0 to 6 cm in 0.75 cm intervals and ZVA classes from 0 to 22.5 in 5º intervals (the first class covering the range

0-2.5º). In the approach (b), only classes for TCWV were used, since the ZVA dependency is explicitly modeled by (3).

Table 3 – List of split-window algorithms tested in this work and their respective references. T_s denotes LST, $C, A_1, A_2, A_3, B_1, B_2, B_3$ are the regression coefficients, T_{11} and T_{12} are the brightness temperatures in the IR 108 and IR 120 channels, ε_{11} and ε_{12} their emissivities and ε the average of both emissivities.

No	Formula	Reference
1	$T_s = C + \left(A_1 + A_2 \frac{1-\varepsilon}{\varepsilon} + A_3 \frac{\Delta\varepsilon}{\varepsilon^2}\right)\frac{T_{11}+T_{12}}{2} + \left(B_1 + B_2 \frac{1-\varepsilon}{\varepsilon} + B_3 \frac{\Delta\varepsilon}{\varepsilon^2}\right)\frac{T_{11}-T_{12}}{2}$	(Wan and Dozier 1996, Freitas et al. 2010)
2	$T_S = C + A_1 \frac{T_{11}}{\varepsilon} + A_2 \frac{T_{12}}{\varepsilon} + A_3 \frac{1-\varepsilon}{\varepsilon}$	(Prata and Platt 1991, Caselles, Coll, and Valor 1997)
3	$T_S = C + A_1 T_{11} + A_2 (T_{11} - T_{12}) + A_3 (1-\varepsilon) + A_4 \Delta\varepsilon$	(Ulivieri et al. 1994)
4	$T_S = C + A_1 T_{11} + A_2 (T_{11} - T_{12}) + A_3 \frac{1-\varepsilon}{\varepsilon} + A_4 \frac{\Delta\varepsilon}{\varepsilon^2}$	(Vidal 1991)
5	$T_S = C + A_1 T_{11} + A_2 (T_{11} - T_{12}) + A_3 (T_{11} - T_{12})(1-\varepsilon_{11}) + A_4 T_{12} \Delta\varepsilon$	(Price 1984)
6	$T_S = C + A_1 T_{11} + A_2 (T_{11} - T_{12}) + A_3 \varepsilon$	(Ulivieri and Cannizzaro 1985)
7	$T_S = C + A_1 T_{11} + A_2 (T_{11} - T_{12}) + A_3 \varepsilon + A_4 \frac{\Delta\varepsilon}{\varepsilon}$	(Sobrino et al. 1994)
8	$T_S = C + A_1 T_{11} + A_2 (T_{11} - T_{12}) + A_3 (1-\varepsilon_{11}) + A_4 \Delta\varepsilon$	(Coll et al. 1997)
9	$T_S = C + A_1 T_{11} + A_2 (T_{11} - T_{12}) + A_3 (T_{11} - T_{12})(T_{11} - T_{12}) + A_4 (1-\varepsilon_{11}) + A_5 \Delta\varepsilon$	(Sobrino et al. 1993)

As for the geostationary satellites, WACMOS-ET uses the SEVIRI/MSG LST product provided by Land-SAF and therefore no further algorithm or product development shall be carried out within this project. The Land-SAF use the GSW proposed by Wan and Dozier (1996) and corresponding to the first formulation in Table 3. The choice of split-window coefficients is based on the pixel view angle and total column water vapour, as obtained from ECMWF operational forecasts. The correction for surface emissivity takes into account the fraction of vegetation cover, also estimated from SEVIRI measurements by the LSA SAF and the IGBP land cover classification (Trigo et al., 2008a).

Since the beginning of operations, SEVIRI LST product underwent several modifications: (i) refinement of the split-window coefficients; (ii) improvement of surface emissivity estimations, from static to dynamic fields based on vegetation cover as described in section 4; (iii) correction of level 1.5 top-of-atmosphere radiances; (iv) improvement of uncertainty estimations. The Land-SAF foresees the re-processing of the entire archive of SEVIRI level 1.5 radiances. Depending on the availability of such dataset, WACMOS-ET will favour the use of re-processed SEVIRI LST instead of the original operational product.

Finally, for MTSAT, only the second approach was applied, as justified in due course; for GOES a different approach needed to be used given the absence of the second TIR channel. The single channel algorithm takes the form:

$$LST = a\frac{T_{TIR1}}{\varepsilon} + b\frac{1}{\varepsilon} + c + d\,(\sec\theta - 1) + \Delta LST \qquad (4)$$

Where a, b, c and d are again empirical coefficients that depend on the atmospheric water vapour content and view angle, and ε is the surface emissivity within the TIR1 channel, determined according to the methodology described in section 4.

4.2.1 AATSR

After obtaining regression coefficients for each GSW using the calibration database, all the models were run using the validation database and the results were compared to the LST values on the SeeBor database. Figure 3 shows a comparison of the results for all the GSWs; the differences between the calculated LST and the one at the SeeBor database were grouped in TCWV classes and for each, a boxplot was calculated, showing the median, the 25 and 75 percentiles and the minimum and maximum error values for each class. The bias and root-mean square error are also indicated in the figure.

In general, algorithm 1 performs better, with the smallest bias and RMSE of about 0.06 K and 0.48 K, respectively. Algorithms 3, 4, 7 and 8 also show lower biases and RMSEs but the intermediate TCWV classes show slightly larger dispersions than algorithm 1. The classes with less TCWV show less dispersion in all the algorithms, but algorithms 2, 5 and 6 seem to show larger errors even at smaller TCWV values. Figure 4 shows the same results, but using approach (b). They look almost exactly the same as the ones obtained with approach (a), with very subtle differences on the biases and RMSEs. This approach is therefore preferred, since it eliminates the need to introduce ZVA classes in the algorithm, thus lowering the chances of getting discontinuities on the resulting LST fields.

4.2.2 MTSAT

Both methodologies used in AATSR, with and without the additional term that takes into account the increase in the optical path with water vapor, were also tested for the MTSAT calibration and validation. The introduction of the angle correction term provided better results, although differences between the two methods were small. Hence, this method was chosen for the same reason as in AATSR. Likewise to AATSR, coefficients were derived for TCWV classes from 0 to 6 cm in 0.75 cm intervals.

A preliminary study included the set of nine algorithms tested for AATSR. In the end, only that of Wan and Dozier (1996) and the one by Coll et al. (1997) showed good results at the calibration/validation phase and both will be presented.

Figures 5 and 6 show a comparison of the results for Wan&Dozier and Coll algorithms. The differences between the calculated LST and the SeeBor skin temperature were grouped in ZVA classes, and each ZVA class grouped in TCWV classes; these results are presented as boxplots. The median, 25 and 75 percentiles, and the minimum and maximum error values are shown for each class. The bias and RMSE are also indicated in the figures.

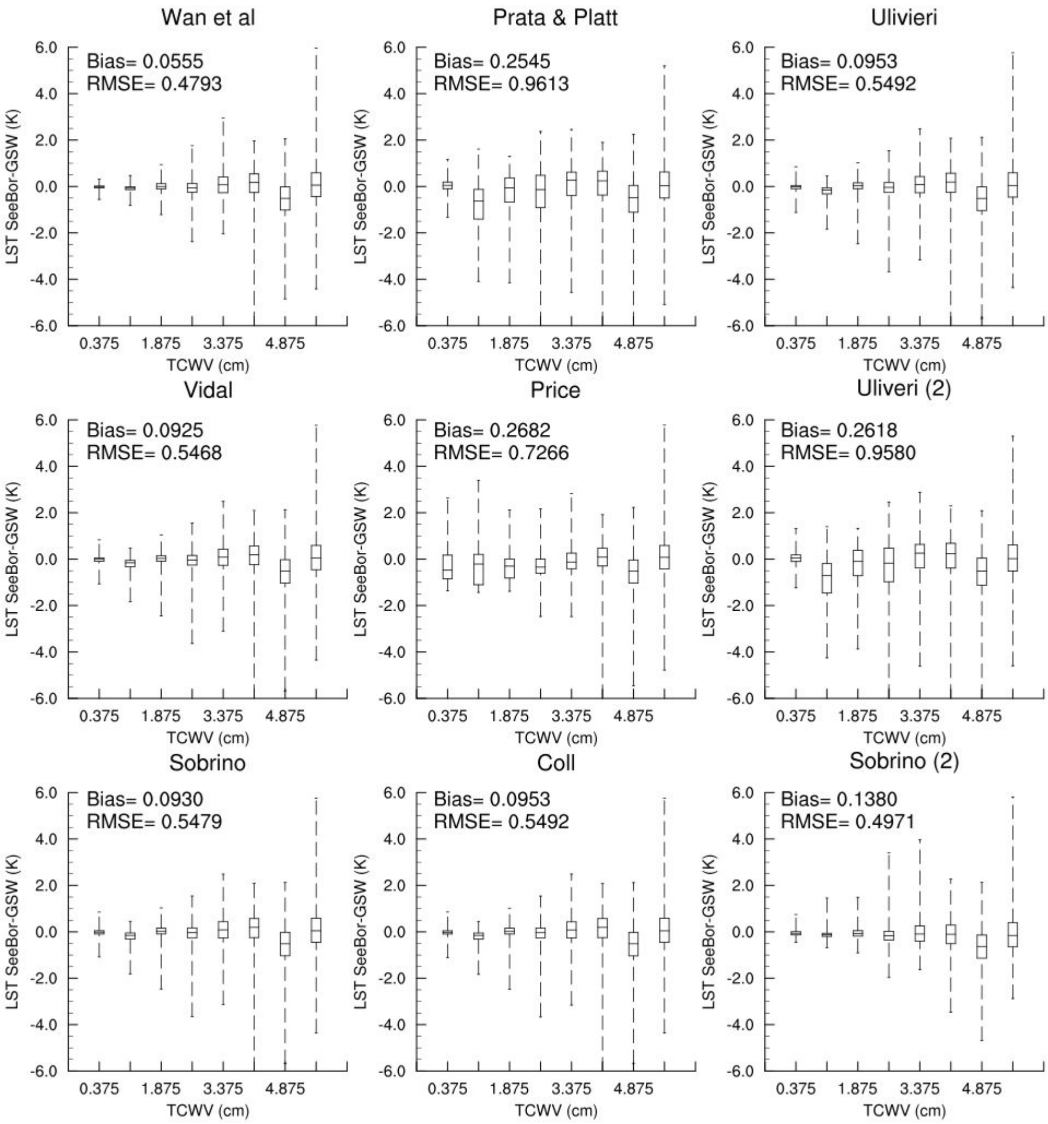

Figure 3 - Validation results using approach (a) for AATSR - see text for details. Each bar is a boxplot of the differences between the LST on SeeBor and the corresponding GSW result, grouped by TCWV class. Also shown are the bias and RMSE for each model.

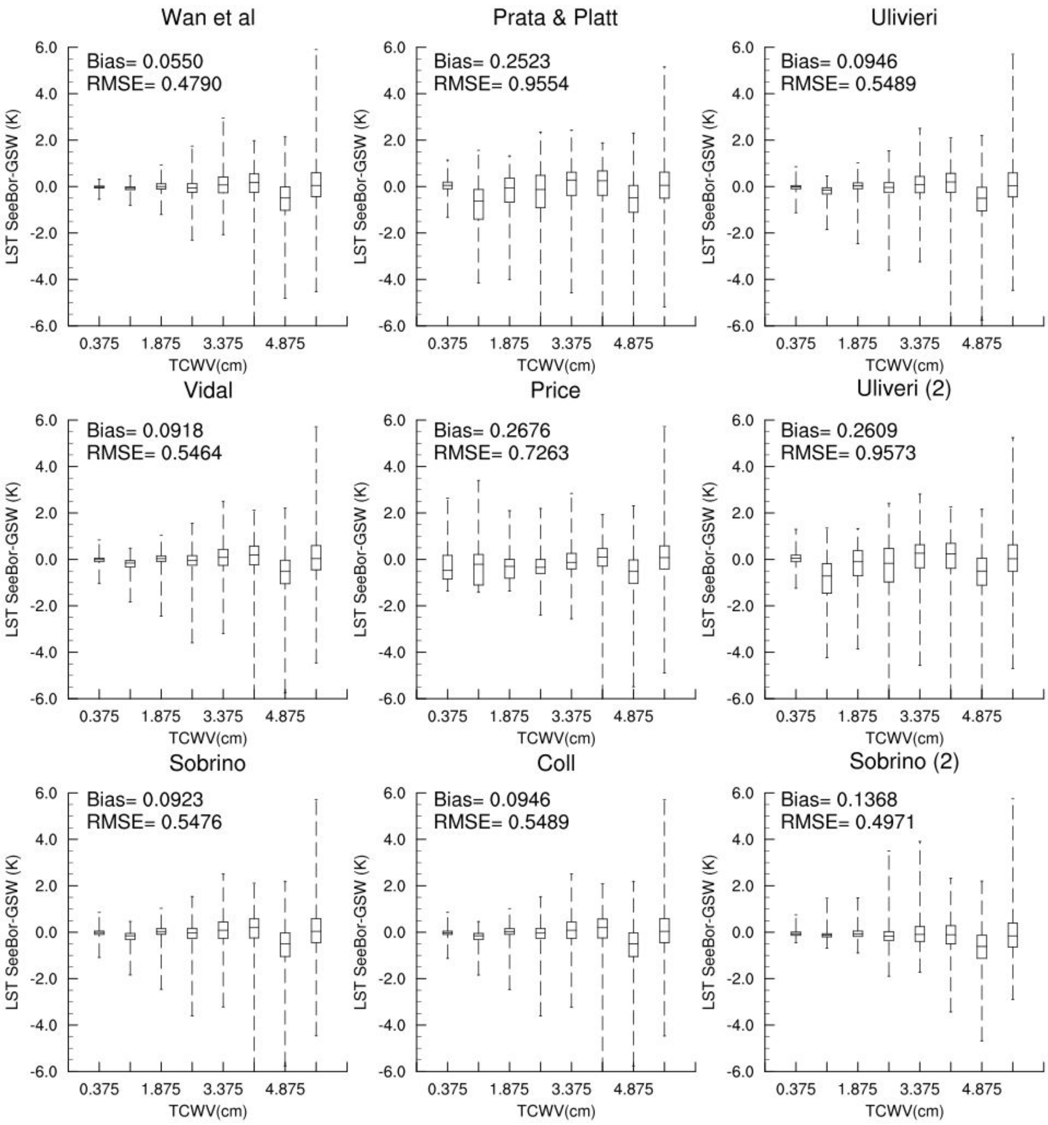

Figure 4 – Same as Figure 3 but for approach (b) (see text for details).

Both algorithms show similar general behaviours: for each ZVA class, the higher the TCWV class, the higher the variance; and, independently of the TCWV class, the higher the ZVA class, the higher the variance. The differences between algorithms are very small, which can be seen by the very low differences in biases and RMSEs for equivalent classes. Nevertheless, Wan & Dozier presents slightly lower differences between computed LST and the SeeBor skin temperature.

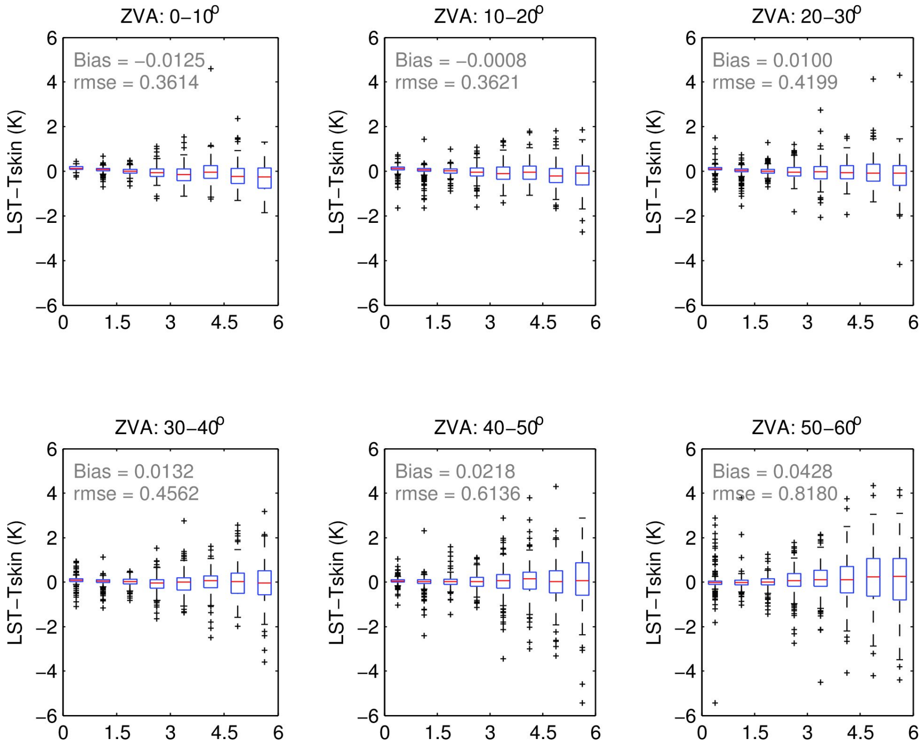

Figure 5 - Boxplots of the differences between MTSAT LST computed with the Wan & Dozier algorithm and Tskin retrieved from the SeeBor database. Differences are plotted according to classes of TCWV (in cm) and are divided into classes of ZVA. Bias and RMSE are indicated.

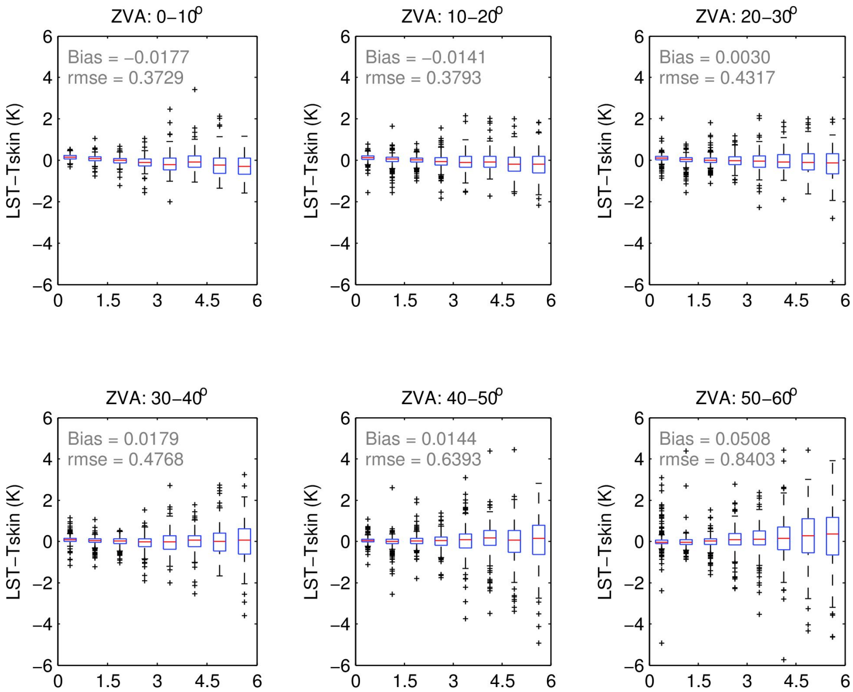

Figure 6 - Same as Figure 5 but for the Coll algorithm.

4.2.3 GOES

Figure 7 is the respective figure for GOES. Notice the different axis scale from Figures 5 and 6. Biases and RMSEs are considerably larger, as would be expected given the much simpler formulation (eq. 4) and given GOES has only one TIR channel as opposed to two in MTSAT. RMSE in MTSAT varies between roughly 0.3 and 0.8 K towards higher zenith viewing angles, whereas GOES presents errors from 1.9 to 2.4 K.

When comparing both model errors according to TCWV and ZVA classes (Figure 8) MTSAT only presents errors higher than 1 K for ZVA>40º and TCWV>3.75 cm, whereas GOES error increases in about 0.5 K for every water vapor class, hardly depending on the angle.

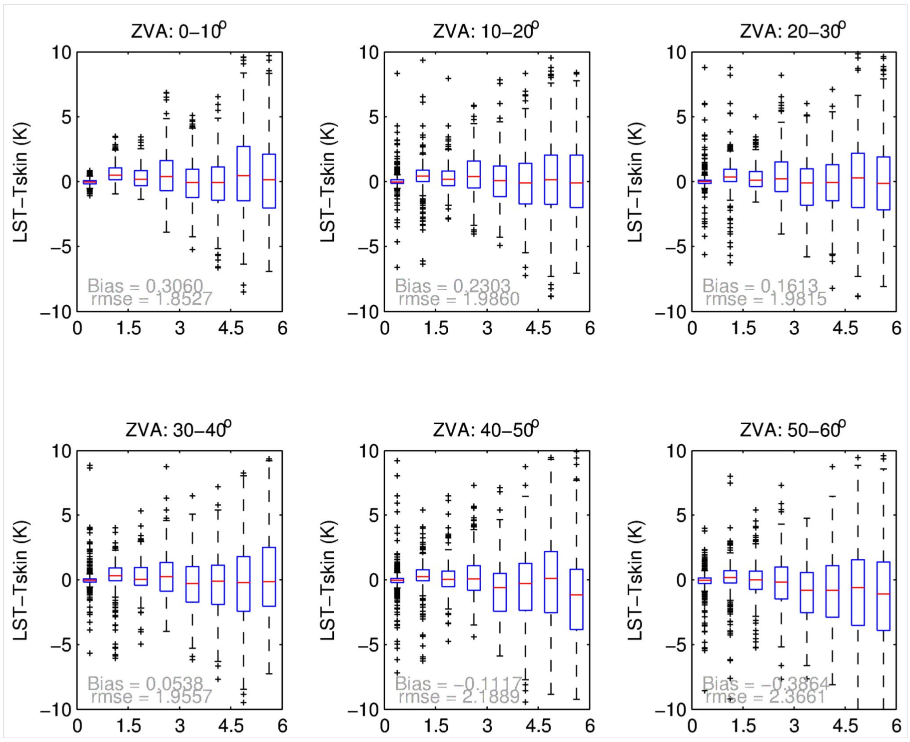

Figure 7 - Boxplots of the differences between GOES LST computed with the Wan & Dozier algorithm and Tskin retrieved from the SeeBor database. Differences are plotted according to classes of TCWV (in cm) and are divided into classes of ZVA. Bias and RMSE are indicated.

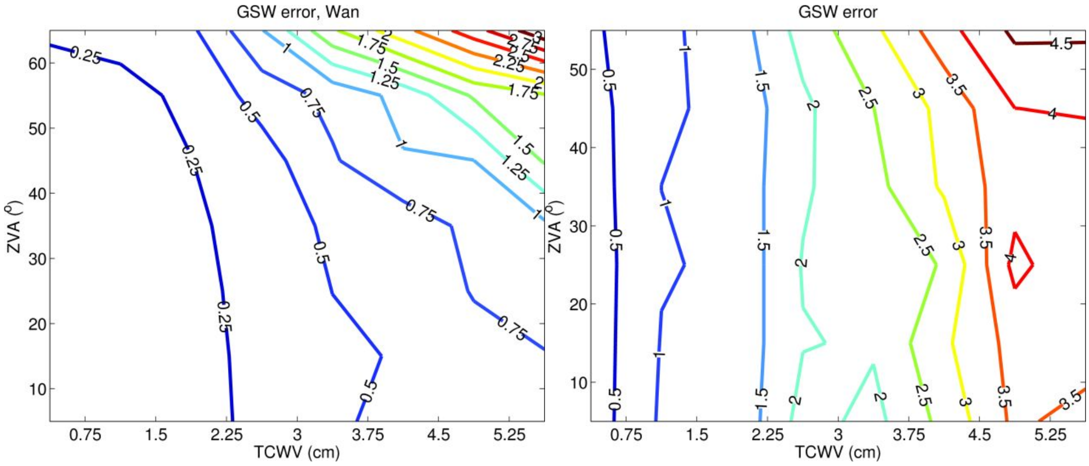

Figure 8 - MTSAT Wan & Dozier (left) and GOES (right) model error.

4.3 Error propagation

All the GSW formulations described above are associated to an error, hereby denoted by σ_{LST}, which mostly comes from the inaccuracy of the inputs and imperfections of the regression itself. The largest sources of uncertainty are the sensor noise, surface emissivity and total column water vapor estimates:

$$\sigma_{LST} = \sqrt{\sigma_{Tb}^2 + \sigma^2 + \sigma_{TCWV}^2 + \Delta LST^2} \quad (5)$$

Each term of (4) is estimated separately using different methodologies. The regression error ΔLST was already discussed in the previous section. Sensor noise σ_{Tb} affects each channel in different magnitudes. In the case of AATSR, the IR 108 and the IR 120 channels are characterized by the same magnitude of the noise temperature of 0.05 K. MTSAT and GOES also have the same error for both channels: 0.16 K and 0.10 K, respectively. To estimate the impact of sensor noise, the brightness temperatures of the validation database were perturbed with Gaussian random noise, with magnitude equal to the respective sensor noise, producing a perturbed database of *Tb*. Each of the GSWs was forced with the perturbed and the unperturbed databases and the uncertainty of the LST was estimated as the variance of the differences between the resulting LSTs that were calculated using each of them.

The same type of methodology was applied to study the emissivity errors. Following Freitas et al. (2010), emissivity perturbations were applied to the emissivities on the

SeeBor database. All the GSWs were run with the original and perturbed values and the differences on LST were used to estimate the error due to emissivity. Depending on the emissivity value, different perturbations of magnitude α were applied (Table 4). This was done because in general the lower the emissivity, the higher is the uncertainty of its determination.

Table 4 – Emissivity perturbation amplitude applied to the SeeBor value, according to its class

Emissivity range	Emissivity perturbation magnitude, α
$0.80 < \varepsilon <= 0.95$	0.03
$0.95 < \varepsilon <= 0.98$	0.02
$\varepsilon > 0.98$	0.006

As previously mentioned, since the SEVIRI data used here were obtained from the Land-SAF operational chain, there is not an error computation.

To estimate the errors due to TCWV, the method is different since this input is used indirectly. This sensitivity is related to the fact that there is a probability of choosing the wrong set of coefficients of a chosen GSW because the forecasted TCWV may lead to a wrong choice of TCWV bin. First of all, one needs to know how likely that situation is, i.e. how frequently does the forecast lead to a wrong choice of bin. To do that, ERA-Interim reanalysis fields of TCWV and Total Cloud Cover (TCC) were retrieved. All the T+12h forecasts of each day 15 of the year 2005 were compared to the corresponding 12h UTC analysis field, filtered by TCC<0.1 to ensure cloud-free conditions.

The probability of getting an analysis TCWV value of $TCWV_{an}$ given a forecast of $TCWV_{fc}$ is given by (see e.g. Figure 10 – left):

$$p(TCWV_{an} \mid TCWV_{fc}) = \frac{p(TCWV_{an} \cap TVCWV_{fc})}{p(TCWV_{fc})} \tag{6}$$

The error caused by forecasting the wrong TCWV is calculated for each GSW using the SeeBor database: for each of the profiles in the database, each GSW is forced with all the possible regression coefficients. As expected, the larger errors are found when large discrepancies between forecasted and analyzed bins are found (e.g. Figure 10 – center).

The expected error is then found by multiplying the error by its probability (e.g. Figure 10 – right).

4.3.1 AATSR

Figure 9 shows how the error in sensor noise propagates in each of the analyzed GSWs. Model 6 seems to be more stable since lower errors are more frequent, especially in the driest atmospheres. Model 5 shows the opposite behavior, with more frequent errors in the 0.2-0.4 bin on the driest atmospheres. The rest of the models show similar and intermediate behavior. In general, the behavior tends to be the same for all models when the only the moister atmospheres are considered, showing that the sensor noise becomes less important compared to water vapor effects.

Figure 10 shows a representation of the emissivity error propagation for all the GSWs, similar to the one on Figure 9. In this case, the general picture is a bit different, with moister atmospheres exhibiting the smaller errors more frequently. It is well known that the sensitivity to land surface emissivity is significantly higher for drier atmospheres, since under moist conditions, the impact of emissivity on the surface-emitted radiance is partially compensated by an opposite effect on the (higher) atmospheric radiation reflected by the surface (Trigo, Peres, et al. 2008). Models 2 and 6 have distinct behaviors in terms of emissivity errors. The error PDF is less sensitive to the TCWV class and they have smaller errors due to emissivity in general. All the others show similar behaviors, with broader error PDFs for lower TCWVs.

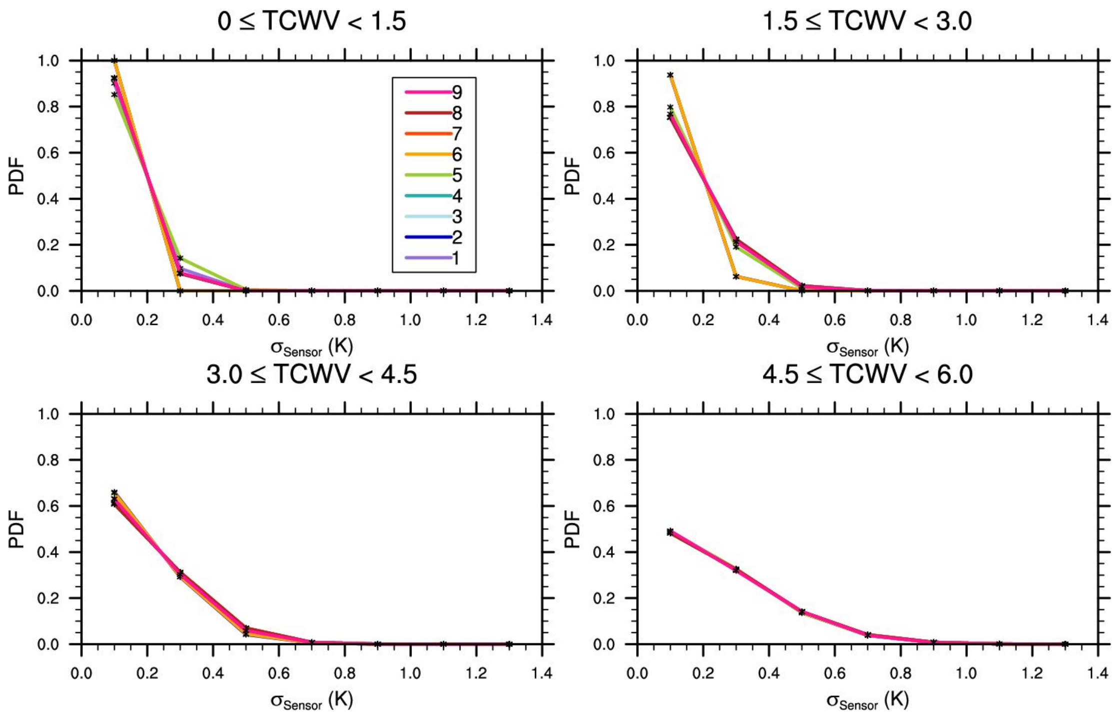

Figure 9 – PDFs of the sensor error propagation in all the GSWs. Each curve represents a GSW in Table 3. Errors were binned in 0.2 K intervals and separated by TCWV classes of width 1.5 cm.

The probability defined in equation (6) is represented in Figure 11 (left). As expected, the error caused by forecasting the wrong TCWV (Figure 11 center) is larger when large discrepancies between forecasted and analyzed bins are found.

It is clear that the expected error (found by multiplying the error by its probability – Figure 11, right) grows with TCWV for all models, with very similar sensitivities between most of them. Again, models 2 and 6 show a distinct behavior, with larger errors in drier atmospheres. Their relatively simpler formulation is probably introducing these biases in lower TCWVs, which are not present in most of the analyzed models.

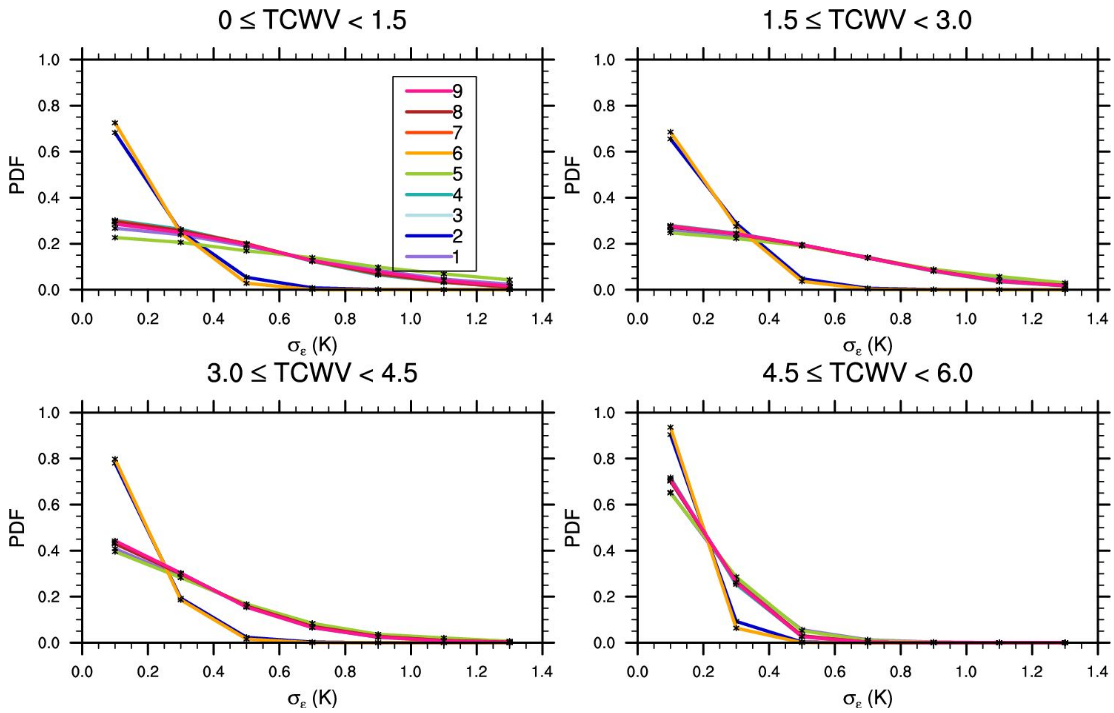

Figure 10 - PDFs of the emissivity error propagation in all the GSWs. Each curve represents a GSW in Table 3. Errors were binned in 0.2 K intervals and separated by TCWV classes of width 1.5 cm.

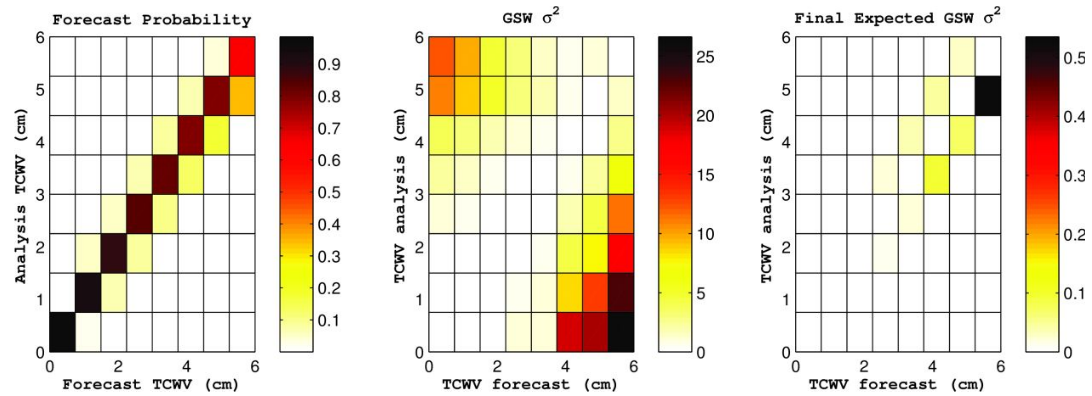

Figure 11 – (left) Probability of getting a given TCWV bin (y-axis), given a forecast on the x-axis. (center) LST Mean Square Error (K^2) caused by getting a wrong TCWV bin forecast – example for GSW 1. (right) Final expected mean square error (K^2), obtained by multiplying the previous plots bin-by-bin – example for GSW 1.

The total LST error is the square root of the squares of each of the individual contributions discussed above and is shown on Figure 13. There is a large homogeneity on the behavior of all models, except models 2, 5 and 6. In general, the total error is dominated by the TCWV influence, as it grows when TCWV grows. Model 9 seems to be the less sensitive model except in two of the TCWV classes. Unfortunately it is a bit more biased against SeeBor "truth" when compared with other models (as shown on Figure 3). Models 2 and 6 are especially sensitive to emissivity (and also model 5 in a lesser extent) and are not recommended for operational use.

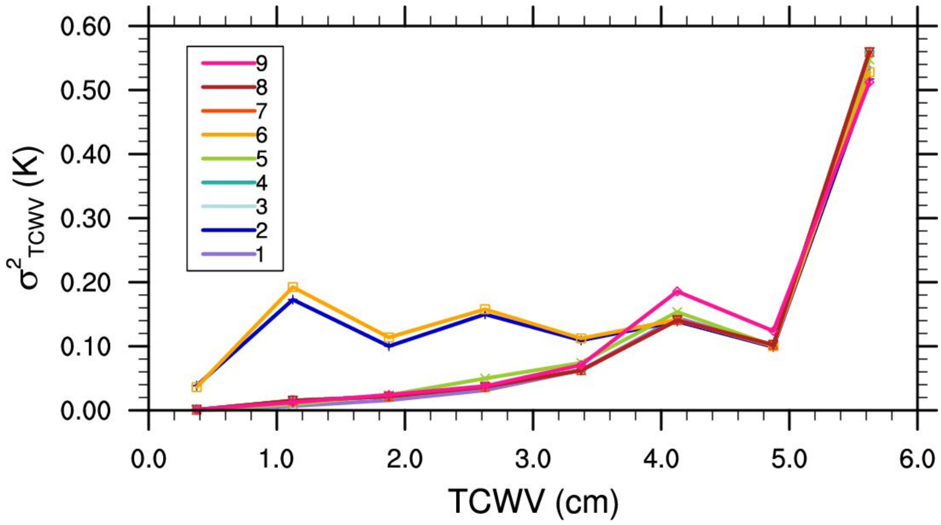

Figure 12 – Mean Square Error (K^2) due to TCWV forecast error for all the GSW, as a function of forecasted TCWV.

4.3.2 MTSAT

Although MTSAT LST was computed with the ZVA being explicitly taken into account, errors are presented as a function of TCWV as well as ZVA. The different error contributions were computed similarly to those of AATSR. For the sensor and emissivity errors, the random generation of noise using the Gaussian distributions with the respective standard deviations was carried out 200 times for each contribution, in order to obtain a greater homogeneity in the results.

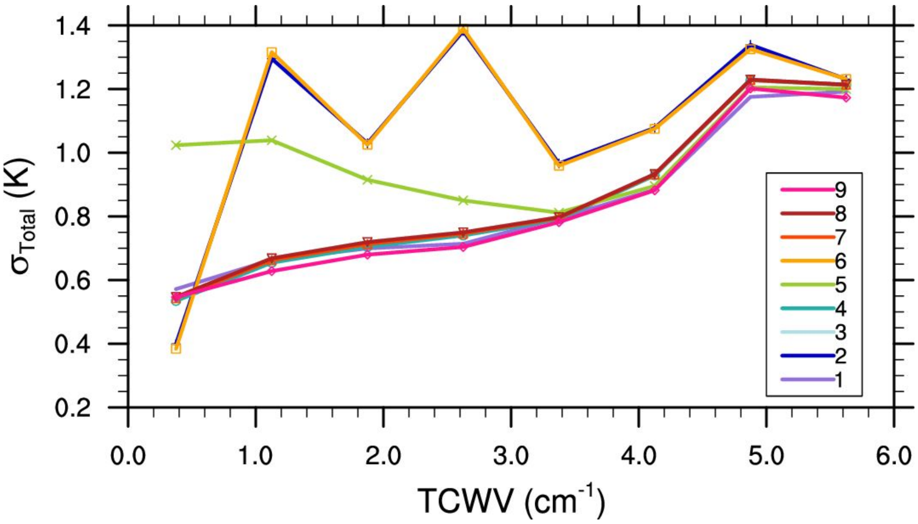

Figure 13 - Total error due to all of the previous contributions (K), as a function of the TCWV class.

Figure 14 presents the sensor error for both algorithms. As expected, the sensor error increases with increasing ZVAs and TCWVs, with values ranging from 0.4 to 1 K. Coll presents overall lower errors for low angles and water vapor content, but slightly higher errors for the last classes of TCWV and ZVA.

Likewise, Figure 15 shows the emissivity errors. Although the error was computed differently for 3 different classes of emissivity, only the average is presented here. The behavior is not as linear; the highest values are found for intermediate water vapor contents (2.25<TCWV<3 cm), up to 1.8 K, and the error decreases towards higher TCWV (errors lower than 0.4 for TCWV>4.5 cm). Wan & Dozier depend more on the angle than Coll, generally showing lower errors for lower TCWVs.

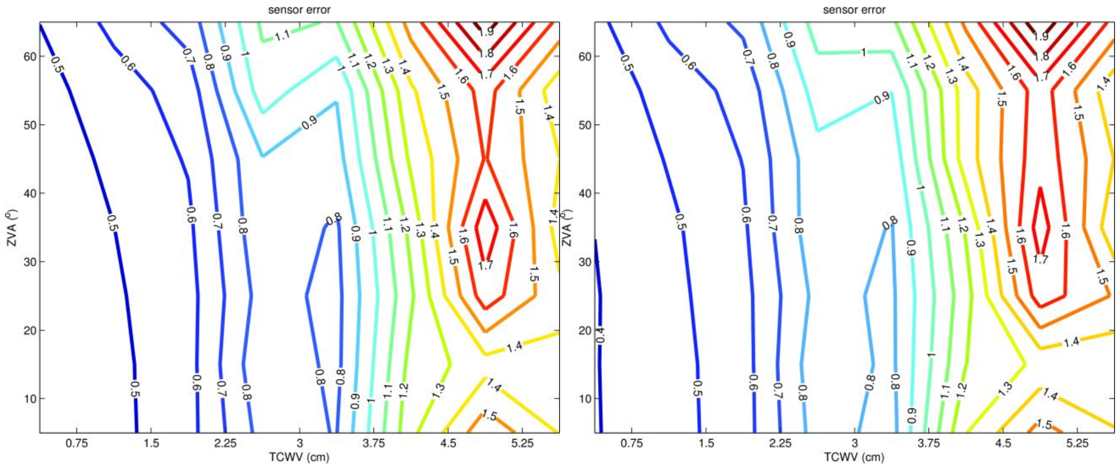

Figure 14 – Sensor error according to TCWV (cm) and ZVA (º) for (left) the Wan & Dozier algorithm and (right) the Coll algorithm.

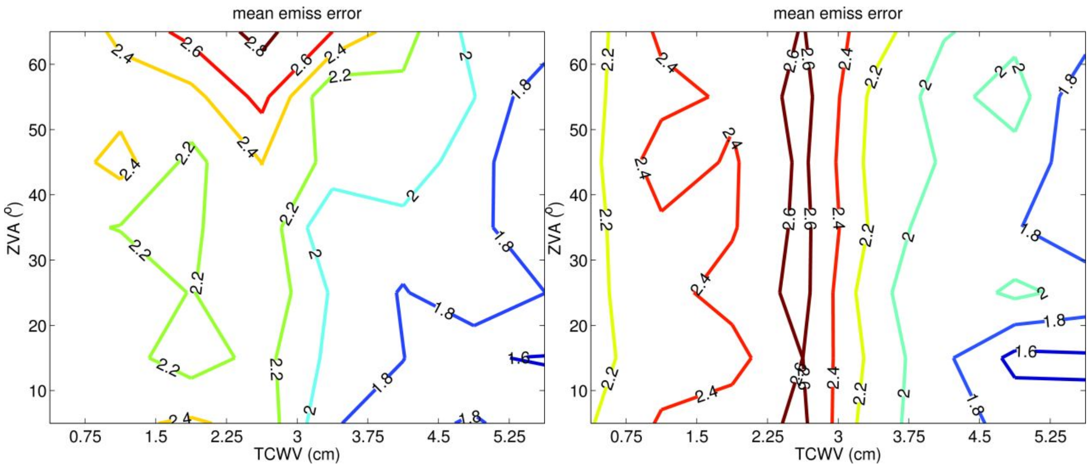

Figure 15 – Emissivity error according to TCWV (cm) and ZVA (º) for (left) the Wan & Dozier algorithm and (right) the Coll algorithm. Error is averaged over emissivity classes.

Figure 16 is similar to Figure 11, but for the two considered algorithms in the MTSAT study. The probability of forecasted TCWV classes in the top panel is the same as the left panel on Figure 10. The most striking differences between the two algorithms are the higher forecasting error of Coll regarding high TCWVs and the higher expected error of Wan & Dozier for the mistaken forecast of the highest TCWV class.

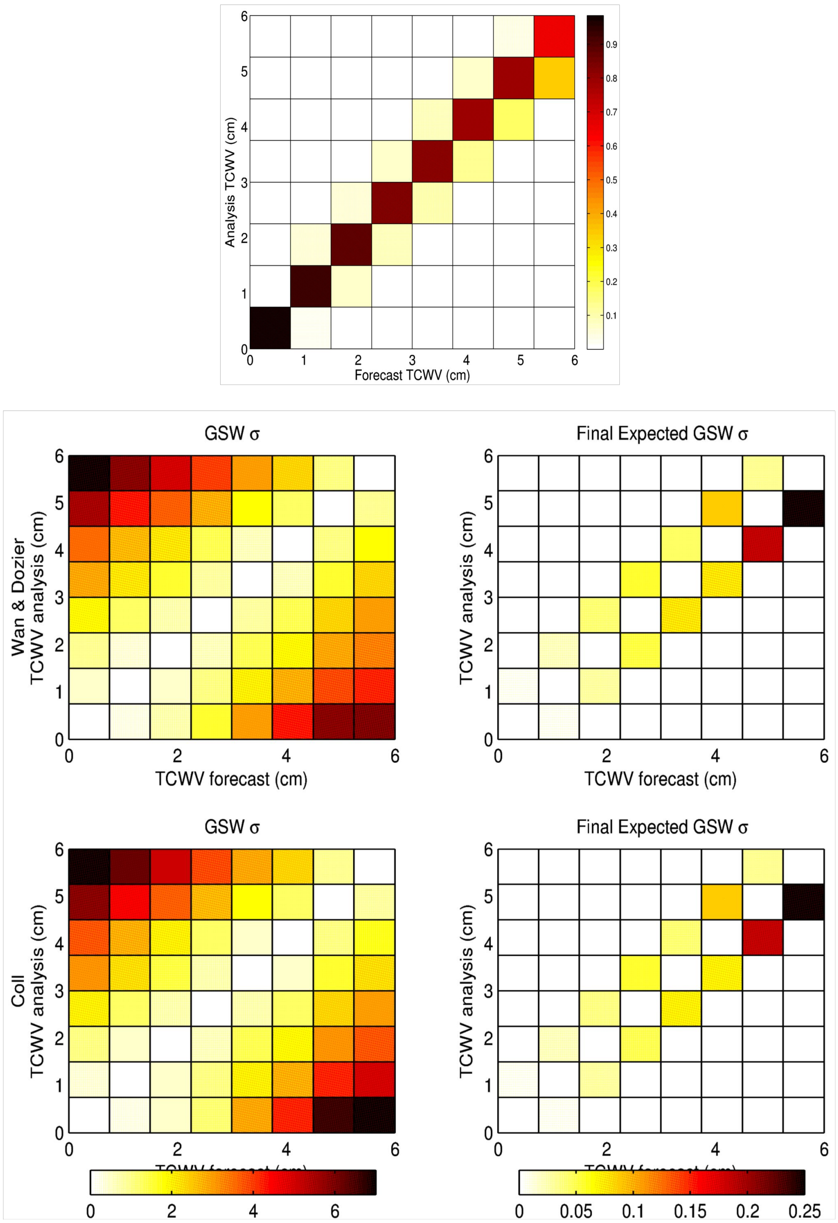

Figure 16 - (top) Probability of getting a given TCWV bin (y-axis), given a forecast on the x-axis. (left) RMSE caused by getting a wrong TCWV bin forecast. (right) Final expected RMSE obtained by multiplying the top and left plots bin-by-bin. The middle panels correspond to the Wan & Dozier algorithm and the lower panels to the Coll algorithm.

When considering the TCWV forecast error as a function of both TCWV and ZVA (Figure 17), the general tendency is increasing errors with increasing water vapor content and angles, as was the case for the sensor contribution. Errors span from 0.05-0.1 K to higher than 0.15 K for TCWV>3.75 cm and ZVA>50º.

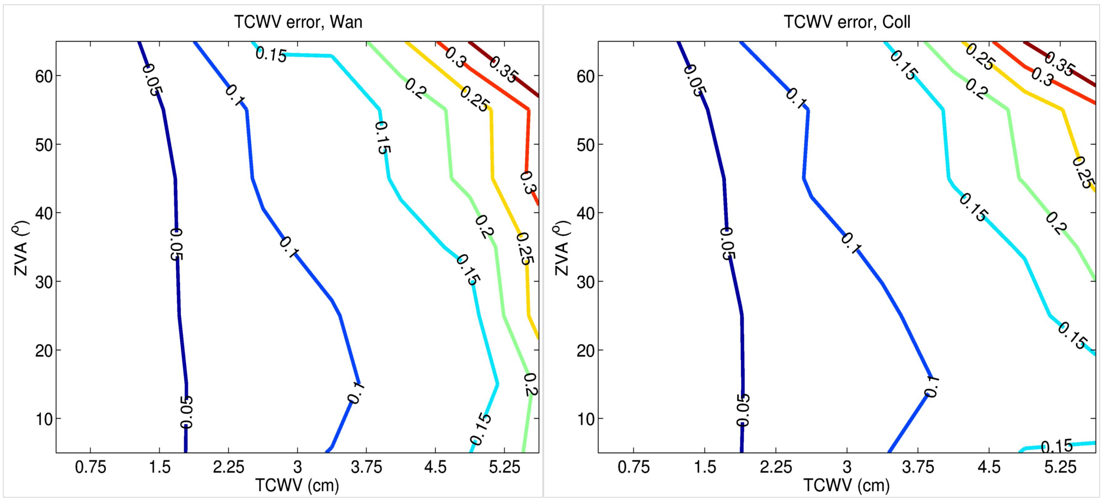

Figure 17 - TCWV forecast error according to TCWV (cm) and ZVA (º) for (left) the Wan & Dozier algorithm and (right) the Coll algorithm.

When summing up all the contributions, the total error (Figure 18) follows the expected behavior of increasing for higher TCWV and ZVA, up to 3.25 K for Wan & Dozier and 3.5 K for Coll. Nevertheless, at intermediate TCWVs the emissivity contribution is noticeable with relative maxima of the order of 1.75 K for Wan & Dozier and 2.25 K for Coll. Coll presents overall higher errors than Wan & Dozier, although the difference between algorithms is very small.

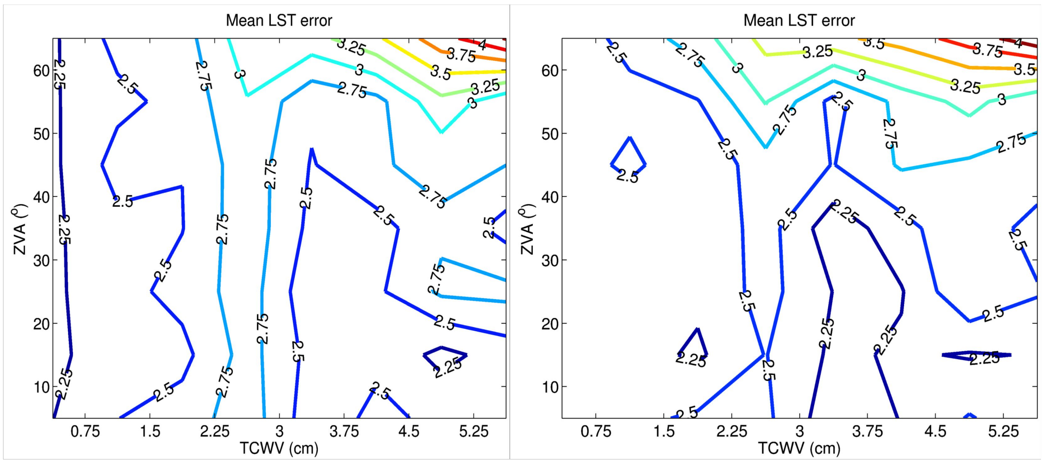

Figure 18 -Total error according to TCWV (cm) and ZVA (º) for (left) the Wan & Dozier algorithm and (right) the Coll algorithm. The error is averaged over the different emissivity classes.

4.3.3 GOES

The same exercise is carried out for GOES, but now only for the Wan & Dozier algorithm with the (sec $\theta - 1$) term added, since for MTSAT it proved to be the one that provided the lowest errors in general.

The errors related to the sensor noise and emissivity (Figure 19) are much lower in GOES than in MTSAT (Figures 14, 15). The sensor errors do not depend on the angle, which is expectable since when testing the algorithm sensibility to perturbations in temperature, only the first term of (4) is affected. The simplicity of this algorithm in comparison to Wan & Dozier is also evident in the emissivity sensitivity. Nevertheless, emissivity errors are again greater at mid-TCWVs and decrease toward greater water vapor content.

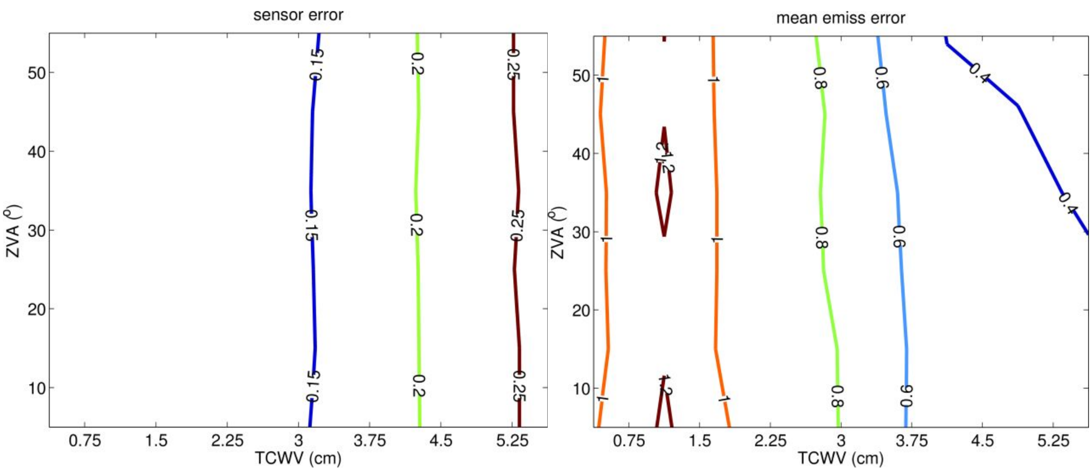

Figure 19 – Sensor error (left) and emissivity error (right) according to TCWV (cm) and ZVA (º). Emissivity error is averaged over emissivity classes.

Although the *d* term was added in order to take into account variations in ZVA, it is an alternate form because originally it was multiplied by the temperature difference in the two channels, which is not applicable in the case of GOES. The figures show that both sensor and emissivity errors do not exhibit a strong dependence on ZVA. Since the *d* term does not depend on temperature or emissivity, the term will not respond to the perturbations introduced when computing the error (a temperature perturbation for the sensor error and an emissivity perturbation for the emissivity error). The errors associated with TCWV (Figure 20) are somewhat different from MTSAT. The errors obtained by attributing the wrong TCWV class are not symmetrical; values are higher when the computed TCWV is lower than the forecast. Moreover, note that the colorbar of the final expected error reaches 0.9, whereas in MTSAT the value range reached only 0.25, in spite of presenting a similar behavior. Consequently, the TCWV associated error in terms of TCWV and ZVA classes is also much higher (Figure 21).

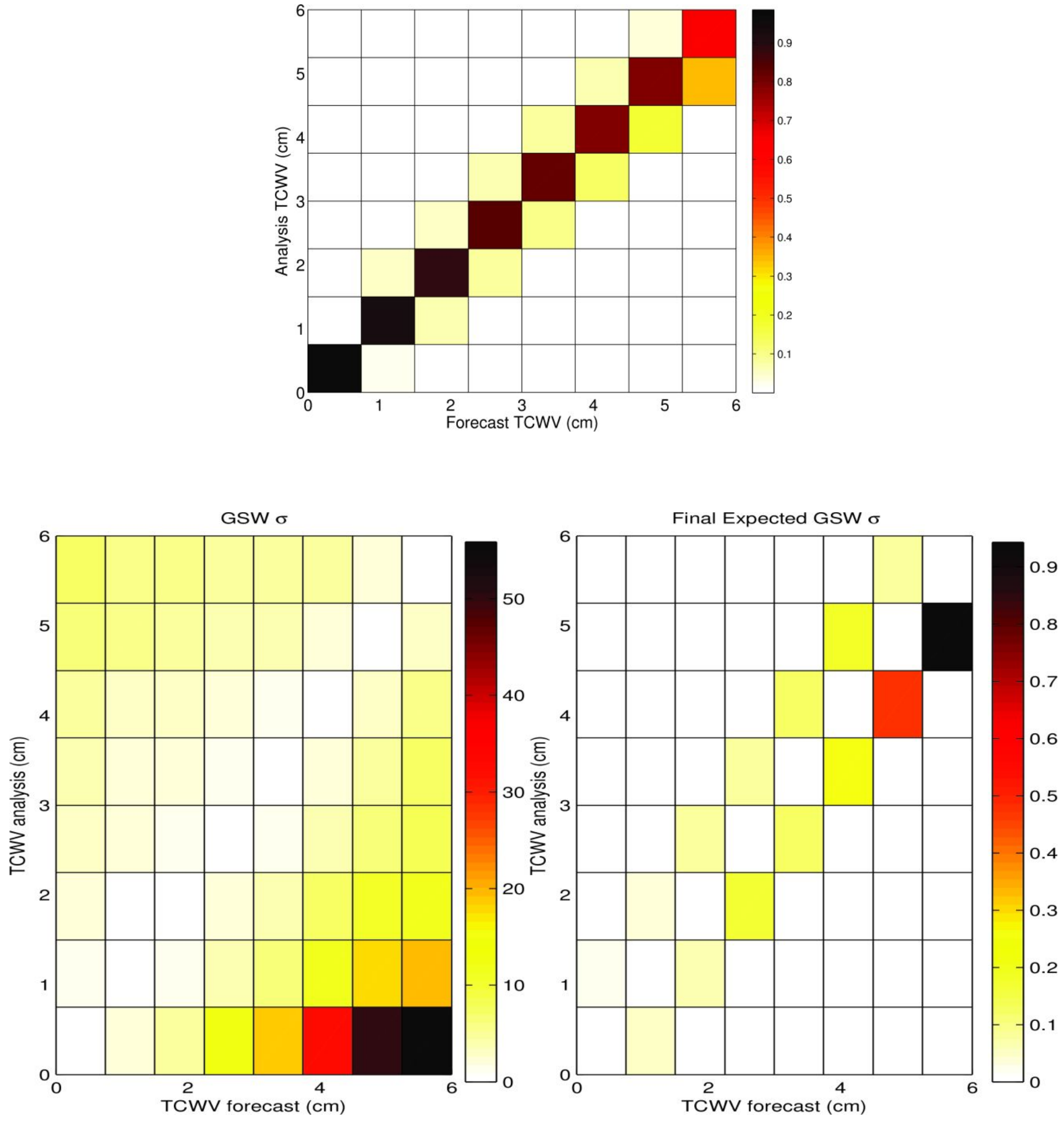

Figure 20 – (top) Probability of getting a given TCWV bin (y-axis), given a forecast on the x-axis. (bottom left) RMSE caused by getting a wrong TCWV bin forecast. (bottom right) Final expected RMSE obtained by multiplying the top and bottom left plots bin-by-bin.

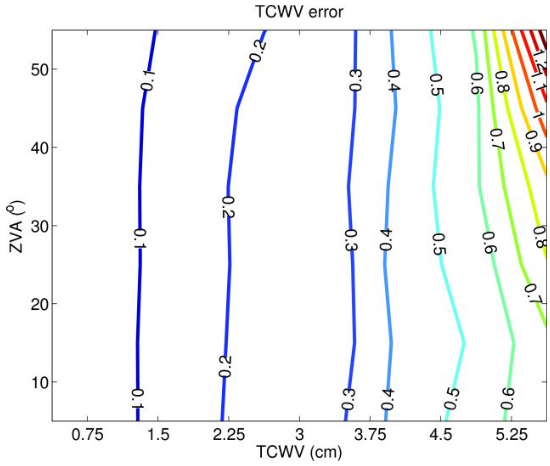

Figure 21 – TCWV forecast error according to TCWV (cm) and ZVA (º) for GOES.

The total error (Figure 22) presents lower values than MTSAT for TCWV<3 cm but higher values for greater water vapor content, for all values of ZVA. For these classes of higher TCWV the differences between sensors reach values as high as 1K.

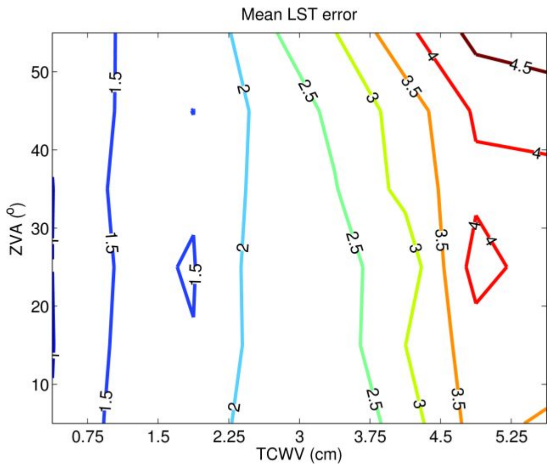

Figure 22 – Total error according to TCWV (cm) and ZVA (º). The error is averaged over the different emissivity classes.

4.4 Algorithm Conclusions

Given the relevance of LST as a climate parameter, and the potential of the AATSR sensor to provide a high-quality database for that parameter, the WACMOS-ET project decided to rethink the LST retrieval algorithm that is currently used.

This work documents the choice of the new algorithm, based on an intercomparison of models currently used in the literature, with emphasis on their performance and sensitivity to input errors.

The algorithm chosen here for sensors with two TIR channels (AATSR and MTSAT) is model number 1 on Table 3 (Wan and Dozier 1996, Freitas et al. 2010), slightly changed in order to include an extra term to directly correct the ZVA effect on the atmospheric correction, lowering the chances of producing discontinuities on the resulting fields due to the use of different regression coefficients for different ZVA classes. The reasons for the choice were: 1) this is the algorithm already in use by Land SAF on their operational chain – and so the L2 data was readily available without any further processing 2) it presents the smaller bias and RMSE when compared to the ground truth LST on SeeBor and 3) it presents a satisfactory sensitivity to input errors. In fact, all models except models 2, 5 and 6 could also be considered as a valid choice if other validation sources were used, since their performance and error sensitivity are very similar to the chosen algorithm.

These conclusions are also valid for MTSAT. After a preliminary analysis of the nine algorithms of Table 3, models 1 and 8 showed the lowest biases and RMSEs when comparing to the SeeBor dataset. Likewise, the approach including a correction term for explicitly modeling ZVA also presented good results, making it a preferable methodology. From the two models, Wan & Dozier proved to be the one with the lowest errors and was therefore the chosen to process LST, such as for AATSR.

For GOES, on the other hand, given that the sensor has only one TIR channel, a different algorithm was put in place. For consistency, the correction term for explicitly modeling the zenith viewing angle was added all the same, but the dependency of the model on the angle is not as striking as in the case of MTSAT. This is due to the formulation itself, particularly the absence of the temperature difference term present on the GSW formulation.

5 Processing chain aspects

5.1 General description of the scheme

In this section we describe the procedures to obtain the LST and its error estimate from the L1 radiances (Figure 23). An initial calibration and validation using MODTRAN simulations as described in section 3 is carried out to obtain the coefficients of the models for each sensor and also the error estimate for each sensor, TCWV class and emissivity range (see Table 4), which are stored on file so they can be used at the processing stage.

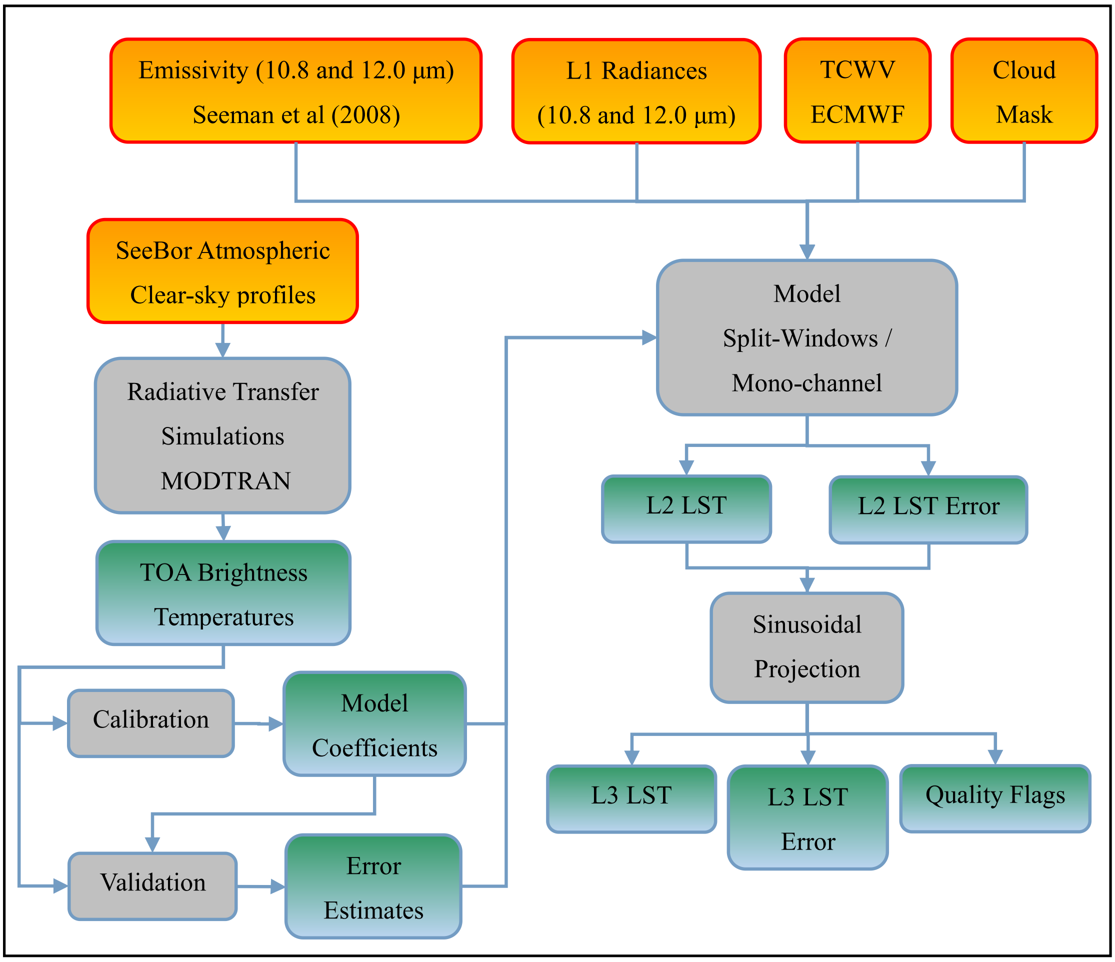

Figure 23 - Flowchart of the processing chain. The orange boxes represent inputs, the green boxes represent outputs and the grey ones represent procedures.

The total column water vapor was retrieved from ECMWF. 3-hourly global fields at 0.75º resolution were available: the 0h, 6h, 12h and 18UTC were analysis, the 3h and 9h are the steps 15 and 21 from the T-12 forecast and the 15h and 21h were the steps 15 and 21 from the T-0 forecast. For each pixel, the time of retrieval is read and the TCWV is interpolated in space and time for the pixel location.

Spectral emissivity was retrieved from monthly files available at 0.05º resolution at the Seeman et al. (2008) database. Solar angles were calculated using spherical geometry routines available from the Land-SAF processing chain and adapted for each of the sensors (except AATSR which contained all the necessary angles at its L1 files).

5.2 Cloud mask

All LST fields are calculated for cloud-free pixels. In the case of AATSR, the L1 radiances that were distributed had already been cloud-flagged, so the user is referred to the AATSR documentation for a complete description of their cloud mask algorithms. For the geostationary sensors, a common algorithm was used, which was the one adapted from the NWC-SAF set of algorithms. Basically the algorithm consists in the comparison of the IR radiances and VIS reflectances of each scene to background values and if the differences are higher than given thresholds, the pixel is considered as cloudy. Additional spatial texture tests are also applied to filter spurious results. Further details on the cloud mask can be found here: http://land.copernicus.eu/global/sites/default/files/products/GIO-GL1_ATBD_Cloud_I1.00.pdf.

5.3 Conversion of GOES satellite counts to radiances and reflectances

GOES files provide 10-bit values of satellite digital counts which need to be converted to scene reflectances and radiances for the visible and infrared channels, respectively. The first step is to convert the 10-bit values to their 16-bit counterparts by multiplying the counts by 32. Then, a linear relationship for each channel is determined empirically at launch time to calculate the quantities of interest. All the parameter values and procedures can be found on this webpage http://www.ospo.noaa.gov/Operations/GOES/calibration/gvar-conversion.html.

Also, the counts are reported in files with grids that were not constant in time. So an additional procedure was to reproject the radiances and reflectances to a common geostationary projection before calculating the LST. All the inputs such as emissivity, TCWV, ZVA, solar angles, etc. were also reprojected to the same grid at the pre-processing phase.

5.4 Reprojection

All the output fields are provided in a sinusoidal projection grid, which is similar to other datasets such as MODIS. In the case of AATSR its grid size is 1/120º (roughly 1 km) and for the geostationary sensors the grid cells are 5 times larger.

To each pixel in the original grids, the nearest pixel of the sinusoidal grid is found using the expressions derived from the sinusoidal grid equations (e.g. http://en.wikipedia.org/wiki/Sinusoidal_projection) The use of this methodology caused artificial discontinuities in the final fields, for no "physical" reason (such as for example the presence of clouds). Therefore, whenever possible every non-filled pixel was filled with an average of at least 4 of its cloud-free neighbors, weighted by the inverse square of their distance (they were flagged accordingly, as described in section 4.4). Despite the grid on each tile is constant for each dataset/sensor, it was chosen to include the latitude and longitude so each file is self-contained and displayable over a map, increasing its usability.

5.5 Quality flags

When the LST cannot be calculated it is filled with a *_FillValue* equal to -30000, as well as all the other output variables. The error flags are stored in the *LST_error* fields: when there is no value to characterize the error of a given pixel (because the LST could not be calculated for the L2 product or because there was no algorithm to provide an error estimate, such as the case of the few years of SEVIRI), a flag is provided. If the pixel is over a water body, the flag is equal to -2. If the pixel is cloudy, the value is -1. There is a third flag, equal to -3, which corresponds to those pixels that were interpolated from their neighbors, as described in the previous section. No error estimate is provided in this case, as the user is free to choose a method of his choice: it may be the largest error from its neighbors, or an average of the errors, etc. Finally, since SEVIRI was not reprocessed in the context of WACMOS-ET, data from the Land-SAF archive was used. The years corresponding to the project had no error estimate, as it was only introduced in the processing chain sometime around July 2008. For this reason, an error flag of -4 is used to mark those pixels with valid LST but no error estimate due to lack of a working algorithm.

A note to the users: the variable *LST_Error* is stored as a 2-byte integer. To decompress and obtain the error as a float, the user must multiply the integers by the provided *scale_factor*. However, the same variable contains the quality flags. As some netCDF libraries apply the *scale_factor* automatically, it is possible that they multiply the quality flag values as well, so caution is recommended when reading this variable. Note that the error value is always a positive number whereas the flags are always negative.

Table 5 – Interpretation of the values stored on the LST_Error field. Values greater than 0 are the error estimate for the valid pixels and values less than 0 are quality flags.

LST_Error	Interpretation
> 0	LST Error estimate (as described in section 3.3)
-1	Cloudy Pixel (see section 4.1)
-2	Non-processed pixel (L1 pixel already masked, e.g. water bodies)
-3	Pixel filled for cosmetic purposes. Interpolated from at least 4 valid neighbor pixels (see section 4.3)
-4	No error estimate available (see section 4.4)

6 Concluding Remarks

The main development of LST algorithm and processing chain within WACMOS-ET targets AATSR. It is our goal to mitigate some of the limitations of the current LST (level 2) AATSR product, namely: the atmospheric correction through the use of the nearest analysis/forecast, in space and time, of the atmospheric water vapor content to each pixel;

(ii) the surface emissivity correction through the use of information on the vegetation variability throughout the year.

LST algorithms for other sensors being considered here are based on development activities carried in other projects, namely Land-SAF in the case of SEVIRI/MSG and Copernicus Global Land in the case of GOES and MTSAT imagers. Since the operational service of the latter does not cover the study period of WACMOS-ET, GOES and MTSAT LST were re-processed for the 2005-2007 period.

The work carried out within WACMOS-ET put into evidence the importance of a careful construction of the database used for the calibration of LST algorithms. Algorithm calibration and verification relies on simulations of TOA brightness temperatures (performed for all sensors under study) for a wide range of atmospheric and surface conditions. The TCWV of profiles in the calibration database is forced to follow a flat distribution in order to ensure that all atmospheric conditions are equally represented in that dataset. In contrast, the statistical distribution of surface and atmospheric variables in the verification database is close to a climatology of the same variables, i.e., they represent their natural occurrence. Using this study as a baseline, the team proposes a standard procedure to build calibration and verification databases.

7 References

Berk, A., G.P. Anderson, P.K. Acharya, J.H. Chetwynd, M.L. Hoke, L.S. Bernstein, E.P. Shettle, M.W. Matthew, and S.M. Adler-Golden. 2000. "MODTRAN 4 Version 2 User Manual." *AIR FORCE RESEARCH LABORATORY, Space Vehicles Directorate, AIR FORCE MATERIEL COMMAND, HANSCOM AFB*.

Borbas, E., S. Seemann, H.-L. Huang, J. Li, and W. P. Menzel. 2005. Global profile training database for satellite regression retrievals with estimates of skin temperature and emissivity. Paper read at Proceedings of the 14th International ATOVS Study Conference, Beijing, China.

Caselles, V., C. Coll, and E. Valor. 1997. "Land surface emissivity and temperature determination in the whole HAPEX-Sahel area from AVHRR data." *International Journal of Remote Sensing* no. 18 (5):1009-1027.

Caselles, V., and J. A. Sobrino. 1989. "Determination of frosts in orange groves from NOAA-9 AVHRR data." *Remote Sensing of Environment* no. 29 (2):135-146. doi: http://dx.doi.org/10.1016/0034-4257(89)90022-9.

Coll, C., E. Valor, T. Schmugge, and V. Caselles. 1997. A procedure for estimating the land surface emissivity difference in the AVHRR channels 4 and 5 Paper read at Remote Sensing Application to the Valencian Area, at Spain.

Dee, D. P., S. M. Uppala, A. J. Simmons, P. Berrisford, P. Poli, S. Kobayashi, U. Andrae, M. A. Balmaseda, G. Balsamo, P. Bauer, P. Bechtold, A. C. M. Beljaars, L. van de Berg, J. Bidlot, N. Bormann, C. Delsol, R. Dragani, M. Fuentes, A. J. Geer, L. Haimberger, S. B. Healy, H. Hersbach, E. V. Holm, L. Isaksen, P. Kallberg, M. Koehler, M. Matricardi, A. P. McNally, B. M. Monge-Sanz, J. J. Morcrette, B. K. Park, C. Peubey, P. de Rosnay, C. Tavolato, J. N. Thepaut, and F. Vitart. 2011. "The ERA-Interim reanalysis: configuration and performance of the data assimilation system." *Quarterly Journal of the Royal Meteorological Society* no. 137 (656):553-597. doi: 10.1002/qj.828.

Dorman, J. L., and P. J. Sellers. 1989. "A global climatology of albedo, roughness length and stomatal-resistance for atmospheric general-circulation models as represented by the Simple Biosphere Model (SIB)." *Journal of Applied Meteorology* no. 28 (9):833-855. doi: 10.1175/1520-0450(1989)028<0833:agcoar>2.0.co;2.

Freitas, S. C., I. F. Trigo, J. M. Bioucas-Dias, and F.-M. Goettsche. 2010. "Quantifying the Uncertainty of Land Surface Temperature Retrievals From SEVIRI/Meteosat." *Ieee Transactions on Geoscience and Remote Sensing* no. 48 (1):523-534. doi: 10.1109/tgrs.2009.2027697.

Freitas, S. C., I. F. Trigo, J. Macedo, C. Barroso, R. Silva and R. Perdigão, 2013: Land surface temperature from Multiple Geostationary Satellites, *Int J. Remote Sens.,* in press, DOI:10.1080/01431161.2012.716925.

Lacaze, R., G. Balsamo, F. Baret, A. Bradley, J.-C. Calvet, F. Camacho, R. D'Andrimont, S. C. Freitas, H. Makhmara, V. Naeimi, P. Pacholczyk, H. Poilvé, B. Smets, K. Tansey, I. F. Trigo, W. Wagner, M. Weiss, 2010. "GEOLAND2 - Towards an Operational GMES Service, first results of the biogeophysical parameter core mapping service. ISPRS Technical Commission VII Symposium, XXXVIII,part 7b, 354-359.

Prata, A.J. 2002. "Land surface temperature measurement from space: AATSR algorithm theoretical basis document." *Contract Report to ESA, CSIRO Atmospheric Research, Aspendale, Victoria, Australia*.

Prata, A.J., and C.M.R. Platt. 1991. Land surface temperature measurements from the AVHRR. Paper read at Proceedings of the 5th AVHRR data users conference.

Price, J. C. 1984. "Land surface temperature measurements from the split window channels of the NOAA 7 Advanced Very High Resolution Radiometer." *Journal of Geophysical Research: Atmospheres (1984–2012)* no. 89 (D5):7231-7237.

Seemann, S.W.; E. E. Borbas, R. O. Knuteson, G. R. Stephenson, and H-L. Huang, 2008: Development of a Global Infrared Land Surface Emissivity Database for Application to Clear Sky Sounding Retrievals from Multispectral Satellite Radiance Measurements. J. Appl. Meteor. Climatol., 47, 108–123. doi: http://dx.doi.org/10.1175/2007JAMC1590.1

Schmetz, J., P. Pili, S. Tjemkes, D. Just, J. Kerkmann, S. Rota, and A. Ratier. 2002. "An introduction to Meteosat Second Generation (MSG)." *Bulletin of the American Meteorological Society* no. 83 (7):977-+. doi: 10.1175/1520-0477(2002)083<0977:aitmsg>2.3.co;2.

Sobrino, J.A., Z.L. Li, M. P. Stoll, and F. Becker. 1993. Determination of the surface temperature from ATSR data. Paper read at Proceedings of 25th International Symposium on Remote Sensing of Environment.

Sobrino, J. A, Z.-L. Li, M. P. Stoll, and F. Becker. 1994. "Improvements in the split-window technique for land surface temperature determination." *Geoscience and Remote Sensing, IEEE Transactions on* no. 32 (2):243-253.

Soria, G., and J. A. Sobrino. 2007. "ENVISAT/AATSR derived land surface temperature over a heterogeneous region." *Remote Sensing of Environment* no. 111 (4):409-422. doi: 10.1016/j.rse.2007.03.017.

Trigo, I. F., L. F. Peres, C. C. DaCarnara, and S. C. Freitas. 2008a. "Thermal land surface emissivity retrieved from SEVIRI/Meteosat." *Ieee Transactions on Geoscience and Remote Sensing* no. 46 (2):307-315. doi: 10.1109/tgrs.2007.905197.

Trigo, I. F., C. C. Dacamara, P. Viterbo, J.-L. Roujean, F. Olesen, C. Barroso, F. Camacho-de-Coca, D. Carrer, S. C. Freitas, J. Garcia-Haro, B. Geiger, F. Gellens-Meulenberghs, N. Ghilain, J. Melia, L. Pessanha, N. Siljamo, and A. Arboleda. 2011. "The Satellite Application Facility for Land Surface Analysis." *International Journal of Remote Sensing* no. 32 (10):2725-2744. doi: 10.1080/01431161003743199.

Trigo, I. F., I. T. Monteiro, F. Olesen, and E. Kabsch. 2008b. "An assessment of remotely sensed land surface temperature." *Journal of Geophysical Research-Atmospheres* no. 113 (D17). doi: 10.1029/2008jd010035.

Ulivieri, C., and G. Cannizzaro. 1985. "Land surface temperature retrievals from satellite measurements." *Acta astronautica* no. 12 (12):977-985.

Ulivieri, C.M.M.A., M.M. Castronuovo, R. Francioni, and A. Cardillo. 1994. "A split window algorithm for estimating land surface temperature from satellites." *Advances in Space Research* no. 14 (3):59-65.

Vidal, A. 1991. "Atmospheric and emissivity correction of land surface temperature measured from satellite using ground measurements or satellite data." *REMOTE SENSING* no. 12 (12):2449-2460.

Wan, Z. M., and J. Dozier. 1996. "A generalized split-window algorithm for retrieving land-surface temperature from space." *Ieee Transactions on Geoscience and Remote Sensing* no. 34 (4):892-905.

Yu, Y., J. L. Privette, and A. C. Pinheiro. 2008. "Evaluation of split-window land surface temperature algorithms for generating climate data records." *Ieee Transactions on Geoscience and Remote Sensing* no. 46 (1):179-192. doi: 10.1109/tgrs.2007.909097.